Active control of circular cylinder flow by affiliated rotating cylinders

WANG JianSheng, XU YuanXin[*] & TIAN YongSheng

Key Laboratory of Efficient Utilization of Low and Medium Grade Energy, MOE, School of Mechanical Engineering, Tianjin University, Tianjin 300072, China

This study puts forward an active control method for circular cylinder flow by placing two small affiliated rotating cylinders adjacent to the main cylinder, and their effects on the drag and lift forces acting on the main cylinder as well as the heat transfer effectiveness are numerically investigated. According to the diameter of the main cylinder the Reynolds number is chosen as Re=200. The well-proven finite volume method is employed for the calculation. The code is validated by comparing the present computed results of flow passing an isolated rotating cylinder with those available from the literature. To describe the present control model, two parameters are defined: the rotation direction of the two small cylinders (including co-current rotation and counter-current rotation) and the dimensionless rotation rate α. In the simulation, the rotation rate α varies from 0 to 2.4. The results indicate that the optimum rotation direction of the subsidiary cylinders, which is beneficial to both drag reduction and heat transfer enhancement, is the co-current rotating (the upper affiliated cylinder spins clockwise and the lower affiliated cylinder spins counter-clockwise). We observe noticeable suppression of the vortex shedding and favorable reduction of the fluid forces acting on the main cylinder as the rotation rate increases. Besides, the pressure and viscous components of the drag force are analyzed. Energy balance between energy cost for activating the rotating cylinders and energy saving by the momentum injection is considered. In addition, the influence of the affiliated rotating cylinders on heat transfer is also investigated. The average Nusselt number is found to increase with the rotation rate.

active control, affiliated cylinders, vortex suppression, drag and lift forces, Nusselt number

1 Introduction

The unsteady viscous flow past a circular cylinder has been extensively studied by employing theoretical, numerical and experimental methods due to its simple geometry and representative behavior of bluff body flow. Flow around chimneys, parallel suspension bridges, heat exchanger pipes and high structures are examples of the bluff body flow in industrial application. A very important characteristic of this flow is the shear layer separation and alternative vortex shedding which leads to considerable fluctuating fluid forces. The wake and the separation region can be suppressed by flow control which reduces unsteadiness and fluctuating forces on the bluff body. Therefore, understanding and controlling wake is of great theoretical and practical importance. An effective control method can save energy, increase the propulsion efficiency, and reduce the induced vibrations of the body. In general, the flow control techniques are classified into two categories. 1) Active flow control strategies in which the flow is controlled by supplying additional power and can be applied without any modifications to the geometrical configuration. For the purpose of wake stabilization, blowing and suction were used as a method of active

---

control on the cylinder surface in refs. [1–4]. In an up-to-date study by Ma and Feng [5], flow control around a circular cylinder by synthetic jets was experimentally investigated. 2) In passive control strategies, flow is controlled by modifying the shape of the bluff body or by appending additive devices such as splitter plate, axial slat, control rod and roughness elements on the body surface [6–10].

In recent years, flow around rotationally oscillating cylinder has been studied extensively by numerical methods [11–15]. These studies cover a wide range of flow conditions such as forcing frequency, oscillation amplitude, Reynolds number, etc. The numerical results predict the qualitative nature of the flow around rotationally oscillating cylinder, including the phenomenon of synchronization at low forcing frequency and drag reduction at high forcing frequency [4]. A large number of systematic experiments have been carried out by Modi and Mokhtarian [16, 17], who have employed rotating cylinders as an integral part of bluff bodies such as buildings and moving vehicles. This control concept has been shown to be remarkably effective and successful in delaying separation. Since momentum is injected into the shear layers by the moving surface, in the literature it is also known as moving surface boundary layer control (MSBC), which functions in the following ways [16]. 1) It retards the growth of the boundary layer by minimizing relative motion between the body surface and the free stream. 2) It injects momentum into the boundary layer. 3) It engenders a region of high suction and thereby accelerates flow in its neighborhood and outside of the boundary layer. 4) It postpones separation and interferes with the evolution of the wake.

In the past decades, many attempts of control algorithms have emerged in the non-linear dynamics and control community such as chaos control, synchronization based control, pinning control, sporadic feedback control, etc. [18–21]. It is of great importance to study the physical mechanism of these control methods from a theoretical standpoint so that they can further be applied to practical problems of engineering interest. In the case of flow past a circular cylinder, vortex shedding is the first global instability mode, which needs to be predicted and controlled before attempting other modes that involve turbulence [22]. In addition, Strykowski et al. [23] have found that the vortex shedding behind circular cylinder could be altered and suppressed altogether over a limited range of Reynolds numbers by a proper placement of a second, smaller cylinder in the near wake of the main cylinder. Therefore, in the present study, an active flow control strategy is proposed to control vortex shedding behind a circular cylinder by means of two small rotary attached cylinders. The Reynolds number based on the diameter of the main cylinder is chosen as Re=200. This Reynolds number is chosen because it is in a laminar flow regime, ensuring the boundary layer separation at the cylinder surface is laminar [24]. The laminar flow over a circular cylinder with Re=200 has been considered by many authors as a

test case, and we choose this Reynolds number to make validation of the numerical code by comparing with available results [25, 26] for flow past a rotating circular cylinder (see section 3.1). The aim of this work is to investigate the effectiveness of the active control method in drag reduction as well as heat transfer enhancement in a theoretical point of view. The physical mechanisms behind the active control method are: 1) The co-current rotation of the attached cylinders retards the growth of the boundary layer by minimizing relative motion between the body surface and the free stream; 2) the rotating cylinders bring extra momentum to the boundary thus delay separation. Even though the numerical results in our work are all in laminar regime, the drag reduction mechanism of this active control method is supposed to be applicable to turbulent flows [16]. Gim et al. [27] presented an experimental study of flow past a cylinder with control rods at the rear stagnation point in a water channel by using PIV (particle image velocimetry) technique. They chose a Reynolds number range of 5000 to 20000. It was observed that a control rod with d/D=0.3 has outstanding effect on reducing the turbulent intensity with vortex shedding strongly suppressed in the near wake. Karabelas [28] computed a flow past a rotating cylinder at Re=140000 by using the Large Eddy Simulation with a rotation rate varying from 0 to 2. He found that as the spin ratio increases, the mean drag decreases and the flow tends to be stable.

2 Numerical model and solution methods

The two-dimensional unsteady governing equations for an incompressible flow can be written as follows:

The continuity equation:

$$\frac{\partial u}{\partial x} + \frac{\partial v}{\partial y} = 0. \tag{1}$$

The momentum equation in the x and y directions:

$$\frac{\partial u}{\partial \tau} + u\frac{\partial u}{\partial x} + v\frac{\partial u}{\partial y} = -\frac{1}{\rho}\frac{\partial p}{\partial x} + v\left(\frac{\partial^2 u}{\partial x^2} + \frac{\partial^2 u}{\partial y^2}\right), \tag{2}$$

$$\frac{\partial v}{\partial \tau} + u\frac{\partial v}{\partial x} + v\frac{\partial v}{\partial y} = -\frac{1}{\rho}\frac{\partial p}{\partial y} + v\left(\frac{\partial^2 v}{\partial x^2} + \frac{\partial^2 v}{\partial y^2}\right). \tag{3}$$

The energy equation:

$$\frac{\partial T}{\partial \tau} + u\frac{\partial T}{\partial x} + v\frac{\partial T}{\partial y} = a\left(\frac{\partial^2 T}{\partial x^2} + \frac{\partial^2 T}{\partial y^2}\right), \tag{4}$$

where x and y are the transverse coordinate and longitudinal coordinate in the Cartesian coordinates, respectively; u and v are the velocity components in the x direction and y direction, respectively; p is the pressure, ρ is the fluid density, v is the kinematic viscosity, T is the temperature, and a=

$\lambda/(\rho c_p)$ is the thermal diffusion coefficient. The Reynolds number is calculated as $Re=U_\infty D/\upsilon$ with U_∞ being the free-stream velocity and D the diameter of the main circular cylinder. A Reynolds number of 200 is used for all the simulations.

It is essential to make the inlet, far-field and outlet boundaries far away enough from the cylindrical zone under consideration so that the boundary conditions will not lead to undesirable effects. The computational model is shown in Figure 1. The diameters of both the two attached cylinders are d=0.1D. The gap between the main cylinder and the attached cylinders is g=0.01D. The location of attached cylinders is suitable, as it is an approximate place to enable tangential suction from the favorable pressure gradient region of the main cylinder and injection into the adverse pressure gradient zone. Price et al. [29] investigated the effect of changing the gap (h) between wall and the main cylinder, ranging from h/D=0 to h/D=2, where D is the diameter of the main cylinder. It was found that the flow around the cylinder with control has little difference with the flow around an isolated circular cylinder for h/D>1.0. In the present simulation, the free stream velocity boundary condition is applied to the inlet: $u=U_\infty$ and v=0. On the surface of the main and attached cylinders, no-slip boundary condition is imposed. The boundary conditions, $\partial u/\partial x = 0$ and $\partial v/\partial x = 0$ are applied to the exit boundary. Symmetry boundary conditions, $\partial u/\partial y = 0$ and v=0, are applied to the far field boundaries. The two attached cylinders are placed at angles of ±120° respectively to the upstream vector direction, right behind the main cylinder (shown in Figure 1).

To simplify description, the rotating direction of the two small subsidiary cylinders is defined as follows.

The case that the upper attached cylinder rotates counter-clockwise and the lower attached cylinder rotates clockwise is defined as counter-current rotation. The case that the upper attached cylinder rotates clockwise and the lower attached cylinder rotates counter-clockwise is defined as co-current rotation (see Figure 1).

To facilitate meshing and speed up the simulation, the whole computational domain is divided into two parts. Finer mesh is employed in the cylindrical zone where the gradients of variables are likely to be very high. After a series of
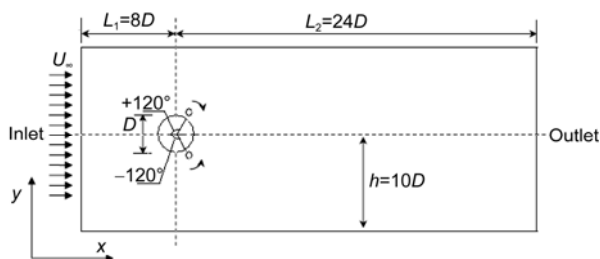
grid independent tests, a meshing method with total elements of 205488 is chosen. A well-proven stabilized finite volume method based on SIMPLE scheme [30] is adopted to solve the incompressible Navier-Stokes equations. The second order semi-implicit scheme is used for the time integration. The spatial discretization is performed on a standard collocated grid using the finite volume method.

3 Results and discussions

3.1 Validation of the code

The drag and lift coefficients are calculated as

$$C_D = \frac{F_D}{\frac{1}{2}\rho U^2_\infty D}, \quad C_L = \frac{F_L}{\frac{1}{2}\rho U^2_\infty D}. \tag{5}$$

The pressure and viscous components of the fluid forces are calculated as

$$C_p = \frac{2(p - p_{\text{ref}})}{\rho U^2_\infty}, \quad C_f = \frac{2\tau_w}{\rho U^2_\infty}. \tag{6}$$

The rotation rate α is defined as

$$\alpha = \frac{\omega D}{2U_\infty},$$

where F_D and F_L are the total drag and lift forces, respectively; τ_w is the shear stress, ω is the angular velocity of the attached cylinder. In addition, symbol "$+\alpha$" represents co-current rotation, and symbol "$-\alpha$" represents counter-current rotation.

The finite volume method, which has been applied to various flow problems, is utilized to solve the incompressible Navier-Stokes equations in the primitive variables formulation. The numerical validations are mainly focused on the fluid forces acting on an isolated rotating cylinder with different rotation rates of α. Figure 2 displays the comparison of the mean drag coefficient obtained by the present numerical calculation with available results in the literature. The computed results are in good agreement with the results obtained by Kang et al. [25] and Stojkovic et al. [26]. The maximum deviation is kept within 5%, which ensures the reliability and accuracy of the present computational model and methods.

3.2 Effects of rotation direction

3.2.1 Analysis of the vortex shedding in the wake region

For a flow past an isolated circular cylinder, a pair of steady and symmetric vortices can be found at a very low Reynolds number. As the Reynolds number increases, the upstream-downstream symmetric vortices disappear and two-attached eddies appear in the wake behind the cylinder. When the


Figure 1 Computational model.
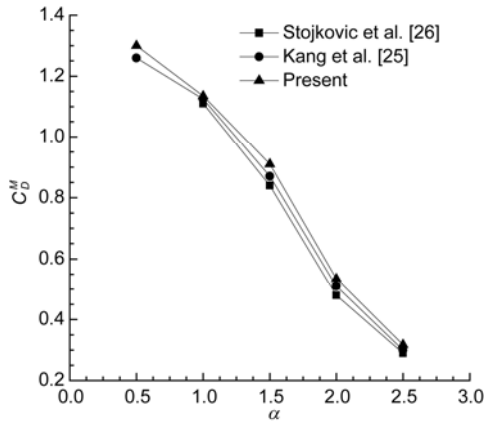
Figure 2 Comparison of mean drag coefficient with existing results of flow past a rotating cylinder for different rotation rates.

Reynolds number exceeds a critical number, alternative vortex shedding can be found to form the famous Karman vortex street. Generally speaking, three characteristic parameters are used to describe the property of the vortex: main direction (the link direction of the two biggest distance summits on the vorticity isoline), center of vorticity (the location of maximum vorticity value), and vorticity isoline shape rate (each vorticity isoline can be transformed into a standard curve).

Figure 3 displays the comparison of vortex shedding structures for counter-current rotation and co-current rotation. It could be observed that in the case of counter-current rotation, the vorticity strengthens gradually as the rotation rate increases, while in the case of co-current rotation, the vorticity weakens with the increasing of the rotation rate. In the former case, as the rotation rate α increases, the vorticity center value of the first shedding vortex behind the main cylinder amplifies and the generated vortices behind the main cylinder become larger and stronger. Moreover, the width of the wake is magnified. Whereas for co-current rotation, the formation of the near wall vortex is delayed and the value of the first shedding vortex weakens. This is due to the fact that additional momentum is injected into the flow separation region by the two co-current rotating cylinders, which postpones the shear layer separation. On the other hand, the attached cylinders hinder the mainstream fluid (flow far from the main cylinder) in the case of counter-current rotation.

3.2.2 Analysis of drag and lift forces

The time variations of the drag and lift forces acting on the main cylinder show significant distinction for different rotation directions. Comparing to the case of a main cylinder with stationary subsidiary cylinders ($\alpha=0$), the mean drag coefficient becomes larger in the case of counter-current rotation, while for co-current rotation, significant reduction is observed and the amplitude of the drag force fluctuation is greatly reduced, as shown in Figure 4(a). Similar varia-
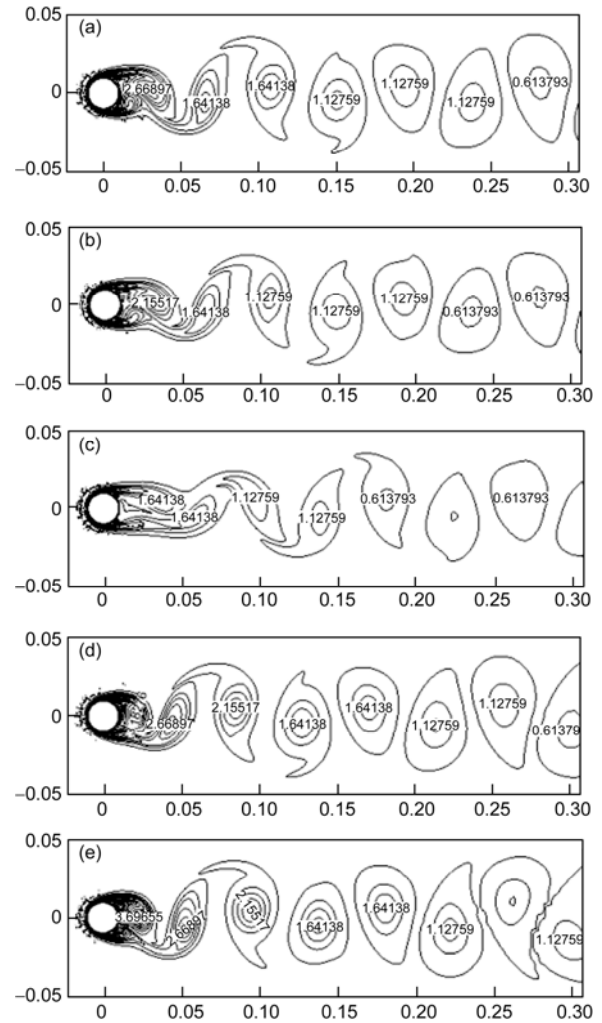

Figure 3 Instantaneous plots of vorticity contours for flow at different control cases. (a) $\alpha=0$; (b) $\alpha=+0.5$, (c) $\alpha=+1.0$; (d) $\alpha=-0.5$, (e) $\alpha=-1.0$.

tion trends could also be found in the plots of lift coefficient; see Figure 4(b). The reduction of the lift force fluctuation agrees well with the results of vortex shedding. The fluctuating lift force is due mainly to the fluctuating pressure acting on the surface of the cylinder caused by the alternative vortex shedding. Table 1 displays the comparison of the mean drag coefficient C_D^M and amplitude of lift coefficient C_L^A for different rotation directions.

Compared with $\alpha=0$, the mean drag coefficient increases by 22.73% for counter-current rotation, yet decreases by 21.8% for co-current rotation at $\alpha=0.5$ and the amplitude of lift fluctuation increases by 39.15%, and decreases by 42.5%, accordingly. For $\alpha=1.0$, compared to $\alpha=0$, the mean drag value and amplitude of lift coefficient increases by 42.6% and 71.83% for counter-current rotation, yet decreases by 45.2% and 85.14% for co-current rotation, respectively.

The influence of rotation direction on wake vortex is in accordance with the impact on fluid forces. The co-current
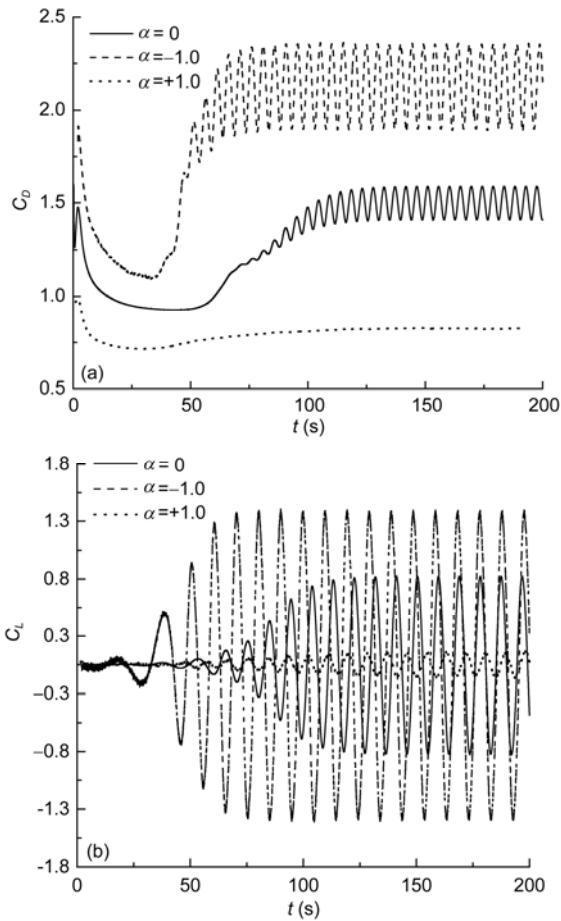
Figure 4 Comparisons of drag (a) and lift (b) coefficient histories in the cases of $\alpha=0$ and $\alpha=\pm1.0$.

Table 1 Comparison of the mean drags and amplitudes of lift coefficients for different rotation directions

	$\alpha=0$	Co-current		Counter-current	
		$\alpha=0.5$	$\alpha=1.0$	$\alpha=0.5$	$\alpha=1.0$
C_D^M	1.500	1.173	0.823	1.841	2.139
C_L^A	0.774	0.445	0.115	1.077	1.330

rotation of the attached cylinders can achieve the purpose of suppressing vortex shedding and reducing the drag and lift forces. The reason is that additional momentum is injected into the shear layers by the placement of the two small rotating cylinders, which delays the formation of the vortex. On the contrary, the counter-current rotation of the attached cylinders fosters the development of vortex and increases the drag and lift forces. It is because the direction of the rotating surfaces is opposite to the mainstream fluid, which results in the increase of the drag force. However, for the co-current rotation, it retards the growth of the boundary layer by minimizing relative motion between the cylinder surface and the mainstream fluid.

3.3 Investigating the co-current rotation of attached cylinders

3.3.1 Analysis of flow field

The computed results show that the two subsidiary rotating cylinders have altered the cylinder wake significantly. The vorticity isoline of wake region, contoured velocity and streamline patterns are shown for different co-current rotation rates of α in Figures 5 and 6. In Figure 5(a)–(f), the simulated results reveal that the center value of vorticity decreases gradually as α increases, the intensity of eddy weakens and the vortex shedding is completely suppressed at $\alpha=2.4$. In Figure 5(g)–(j), when α is relatively low, eddies still exist in the cylinder wake, yet the width of wake stream is reduced. With the increase of α, the periodical vortex shedding is suppressed due to the weakening of the instability in the near wake zone, making it hard to form circulation into the shear layer. However, the convective instability still persists in the far wake region. The streamline patterns show that the sine-shaped fluctuation of wake streamlines tends to become mild as α increases, as shown in Figure 6. The streamline becomes almost straight at $\alpha=$ 2.4, revealing the wake is stable.

3.3.2 Analysis of drag and lift coefficients

It is important to note that the total fluid forces are made up of two components, namely, the viscous (or skin friction) component and pressure component. The total drag coefficient C_D is largely dependent on the pressure component due to flow separation and this separation could be delayed by a moving (rotating) wall. As proposed by Homescul et al. [31], separation is completely eliminated on one side of the cylinder where the moving wall and the free stream move in the same direction and separation only develops incompletely on the other side of the cylinder. In the present study, for co-current rotation of the attached cylinders, the flow separation can be postponed by reducing the velocity difference between the cylindrical zone and the free stream. Consequently, the drag force acting on the main cylinder decreases greatly. Figure 7 shows the variation of the drag and lift coefficients with the rotation rate α. It can be found in Figure 7 that the amplitudes of lift and drag coefficients decline gradually with the increasing α and the fluctuation of lift and drag coefficients tends to disappear due to the increase of stability in the near wake region. Figure 8 presents the variations of the mean drag coefficient and amplitude of the lift coefficient fluctuations at different rotation rates. Compared with $\alpha=0$, the mean drag coefficient for $\alpha=2.4$ is decreased by 78.67%. The declining speed of the lift coefficient is faster than that of the drag coefficient when the rotation rate is relatively low ($\alpha<1.0$), while in the case of a higher α, the lift fluctuation tends to disappear. This tendency corresponds well to the flow field of vortex shedding, in other words, the lift forces disappear in the
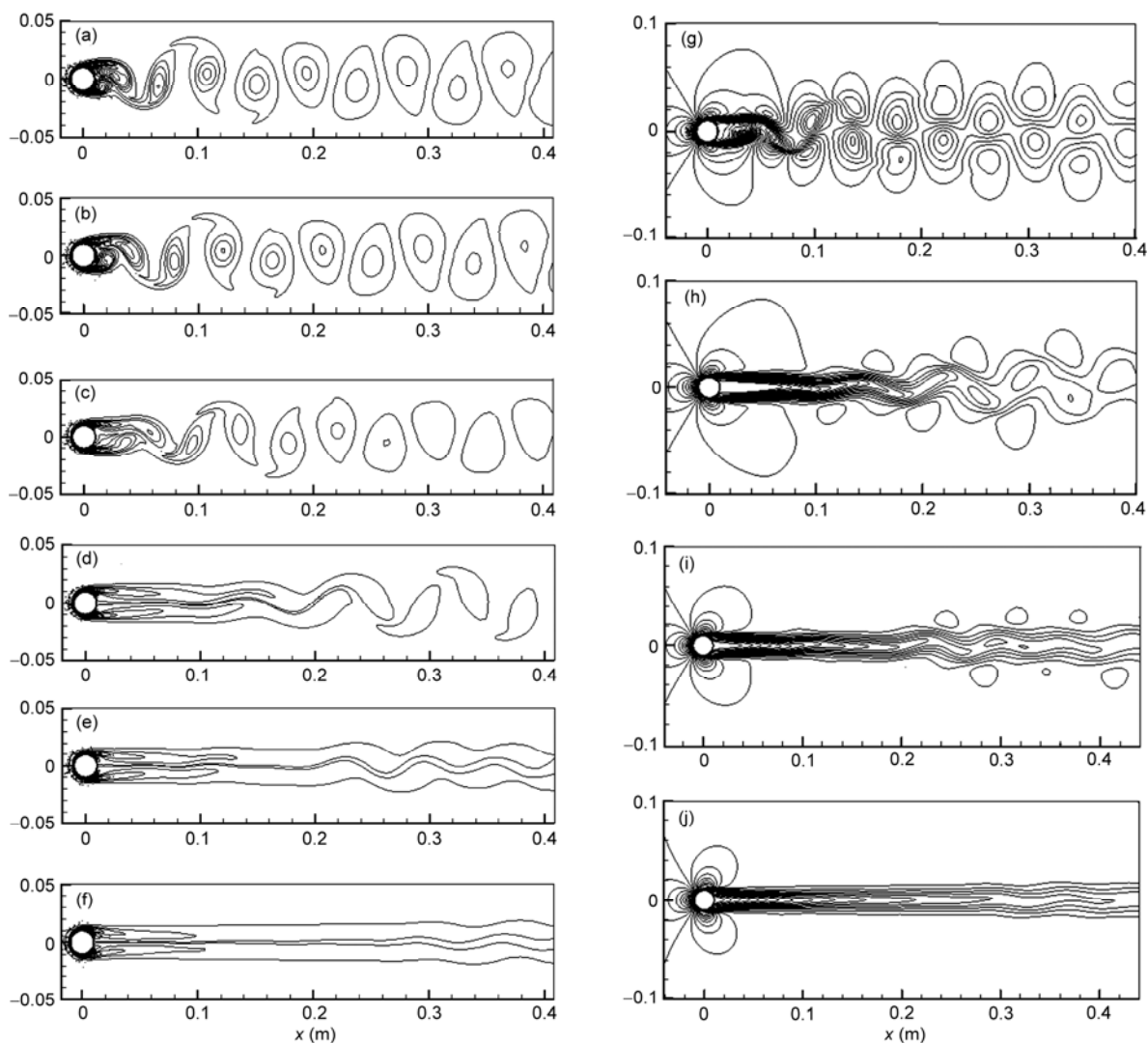
Figure 5 Vorticity isolines for different rotation rates: (a) α=0, (b) α=+0.2, (c) α=+1.0, (d) α=+1.5, (e) α=+2.0, (f) α=+2.4. Contoured velocities for different rotation rates: (g) α=+1.0, (h) α=+1.5, (i) α=+2.0, (j) α=+2.4.
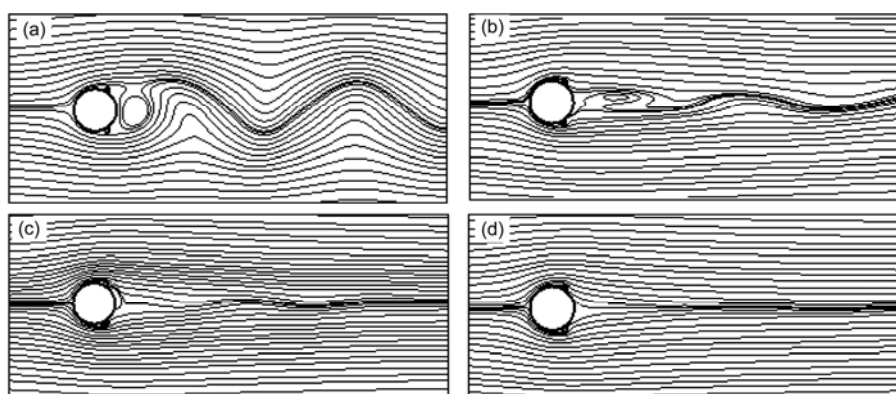
Figure 6 Streamline patterns for different rotation rates: (a) α=+0.2, (b) α=+1.5, (c) +α=2.0, (d) α=+2.4.

cases where the vortex is suppressed. On the other hand, the mean drag force declines all along with the increasing α. With the increase of the rotation rate, vortex shedding which induces the fluctuating forces on the cylinder surface is gradually suppressed, resulting in the remarkable reduction of the drag and lift forces. When the flow wake
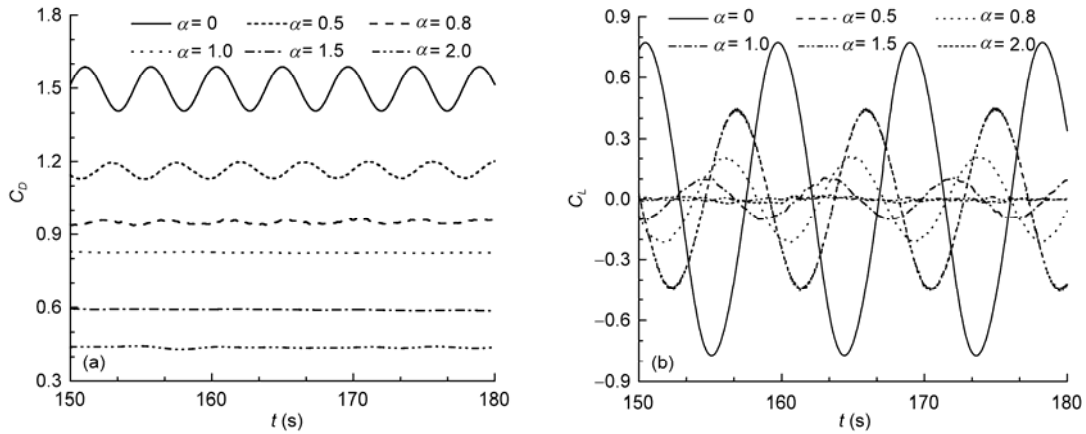
Figure 7   Comparison of drag (a) and lift (b) coefficient histories for different rotation rates.
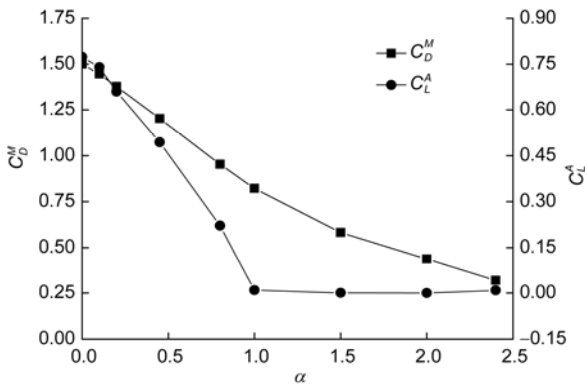

Figure 8   Variations of mean drag coefficient and amplitude of lift coefficients for different rotation rates.

Figure 9   Percentages of pressure and viscous components for different rotation rates and directions.

becomes stable at a higher α, the lift coefficient is almost negligible.

3.4   Discussion of the pressure and friction components of drag force

As mentioned in the above analysis, the total drag force is made up of skin friction component C_f and pressure component C_p, which is often expressed as

$$C_D = C_p + C_f.$$

The pressure component of the fluid force is obtained by integrating the pressure acting on the body faces in the x and y directions, and depends on the shape of the immersed body. Similarly, the viscous component is calculated by integrating the shearing forces acting on the body faces in the x and y directions [10]. The pressure component which is also described as the pressure difference between the high pressure in the front stagnation region and the low pressure in the rear separated zone contributes largely to the total drag force. In Figure 9, the histograms about the percentages of friction and pressure drag show the leading role of the pressure component in the drag force. For co-current
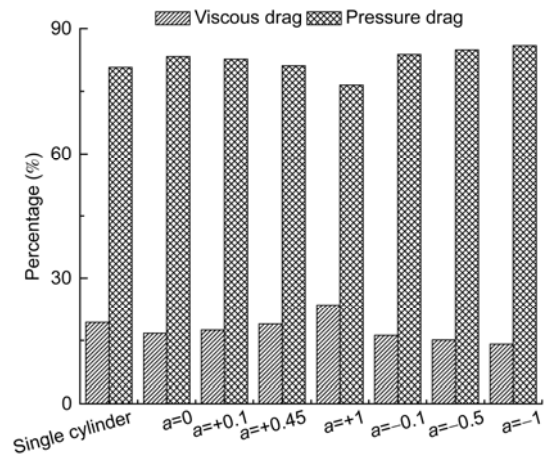
rotation, the percentage of pressure drag reduces gradually as α augments, while the percentage of friction drag rises. For counter-current rotation, comparing to co-current rotation, the variation trends of friction and pressure drag percentage are opposite. Because of the dominating role of the pressure component, it determines the variation trend of the total drag acting on the main cylinder. Figure 10 demonstrates the drag force comparison between a cylinder without control (single cylinder) and the controlled cases at different rotation rates, by displaying the pressure and friction coefficients periodically.

As is shown in Figure 10, the pressure and friction drag are greater than those of the single cylinder for relative low rotation rates. However, both the pressure and friction drag experience favorable reduction when the rotation rate is high enough. In addition, the periods of pressure change are different for the single cylinder and cylinder with control, which should not be neglected. Figure 11 displays the comparison of pressure coefficient and viscous coefficient variations in one period for different rotation rates. It can be seen that the frequency of vortex shedding amplifies at the
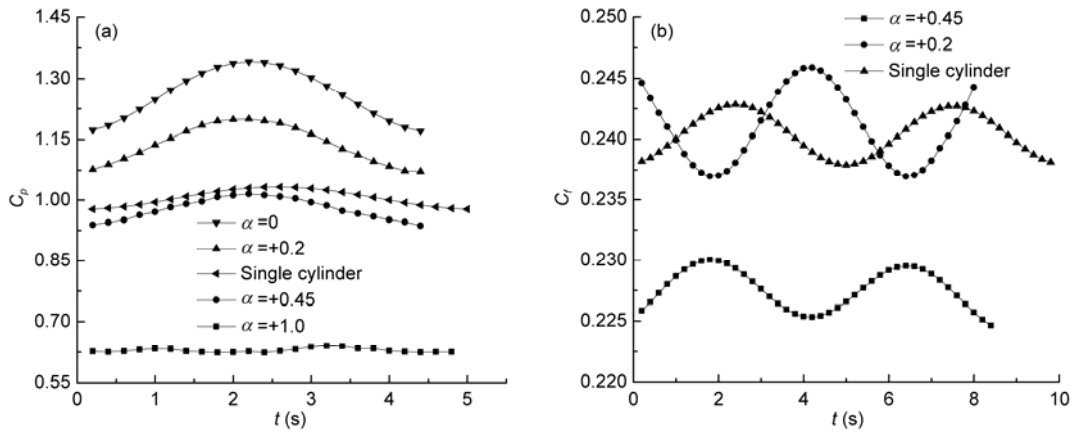
Figure 10   (a) Comparison of pressure coefficient (C_p) variations in a period for different rotation rates; (b) comparison of viscous coefficient (C_f) variations in two periods for different rotation rates.
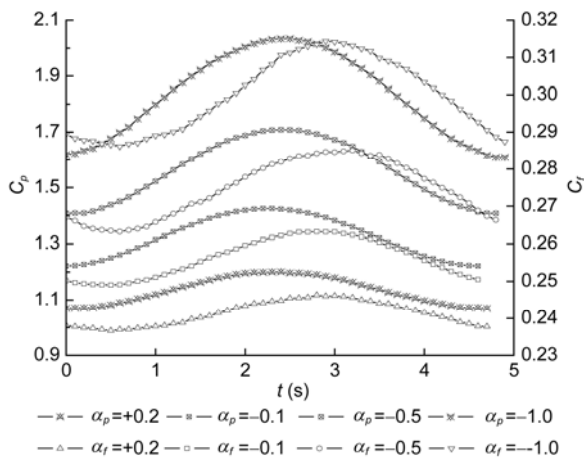
Figure 11   Comparison of pressure coefficient (C_p) and viscous coefficient (C_f) variations in one period for different rotation rates.

relative low rotation rate ($+\alpha$). As for the case of counter-stream rotation ($-\alpha$), the pressure and friction coefficient enlarge increasingly along with the increasing rotation rate. Moreover, phase position is inconsistent with the periodical sine fluctuation between the pressure coefficient and the friction coefficient. The changing speed of friction drag is slightly slower than that of the pressure.

Figure 12 displays the velocity distribution along the positive *x*-axis behind the main cylinder in different rotation directions and at different rates. The velocity of rear region close to the main cylinder reduces gradually along the axial direction with the increasing co-current rotation rate ($+\alpha$), and notable reduction is found at $\alpha=1.0$ (Figure 12(a)). However, the velocity increases at the location far away from the cylinder zone. For counter-stream rotation, the velocity distribution along *x*-axis in the near wake is completely different from in the co-current rotation (Figure 12(b)). The velocity in the wake region close to main cylinder amplifies as α becomes larger. Whereas the velocity decreases in the region far away from the main cylinder,

especially for $\alpha=1.0$.

Figure 13 shows the distribution of local pressure coefficient on the main cylinder. For $\alpha=0$, the pressure at the rear of the main cylinder is lower than that of the single cylinder, so the pressure difference between front stagnation region and the rear zone amplifies. For co-current rotation of the attached cylinders, the rear pressure of the main cylinder increases remarkably as α increases. As a result, the pressure difference between the front and rear zones decreases significantly. The pressure difference also decreases between the upper and lower faces of the main cylinder because of the weakening of the wake oscillation. Whereas in cases of counter-current rotation, the rear pressure of the main cylinder drops as α increases, consequently the amplification of the pressure difference between the front and rear walls (see Figure 13(b)).

3.5   Cost function analysis

According to the definition, active control generally requires external energy to activate the control devices. It is then essential to ensure the energy balance (difference between gain and loss of energy owing to the control) to be positive. Based on the experimental studies of Beaudoin et al. [32, 33], the electric power cost in the measurements is a quadratic function of the rotation speed (ω). And they observed that the electric power does not depend on the flow velocity, given by the following equation:

$$Pe = 2\beta\omega^2, \tag{7}$$

where the constant 2 represents the presence of two small control cylinders placed in the simulated model. The parameter β is obtained by fitting and regression of the experimental data. According to the experimental studies of Beaudoin et al. [32], we can obtain a value of $\beta=0.0008$ W/ $(\mathrm{rad\,s}^{-1})^2$ by adopting a similar procedure (the value chosen through a similar experiment).
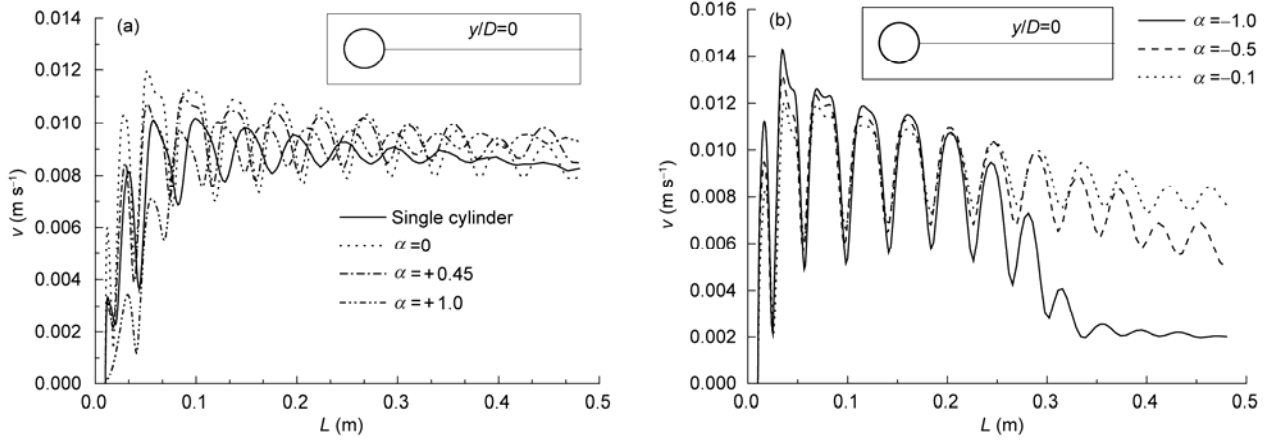
Figure 12 Velocity distributions along *x*-axis behind the main cylinder. (a) Co-current rotation; (b) counter-current rotation.
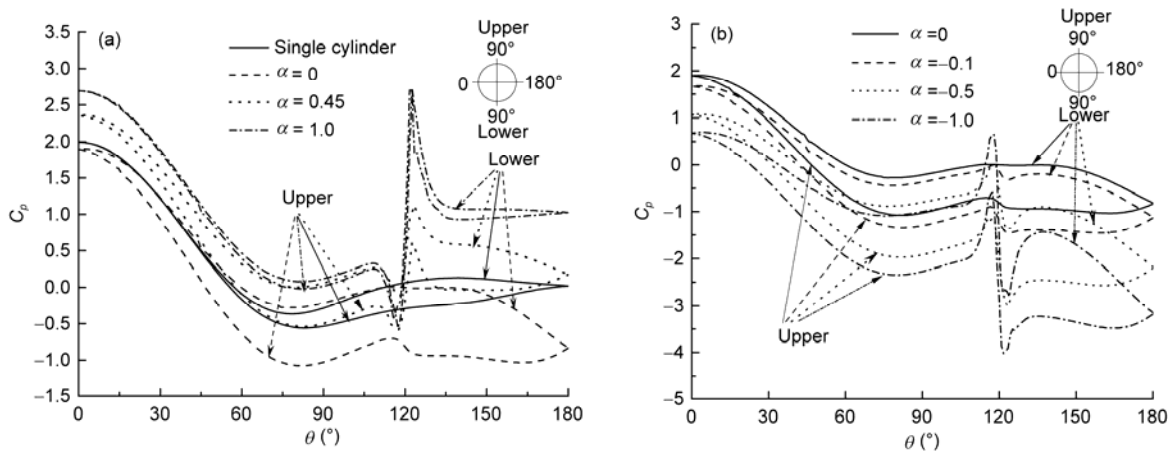

Figure 13 Distributions of pressure coefficient on the main cylinder surface. (a) Co-current rotation; (b) counter-current rotation.

Figure 14 illustrates the variations of mean drag coefficient (C_D^M) and net drag savings ($\Delta C_D^M = C_{D,\text{Single}}^M - C_D^M$) at different rotation rates of α. Figure 15 shows the electric power consumption and net drag savings as α increases. It is displayed in Figure 16 that the proportion of the net drag
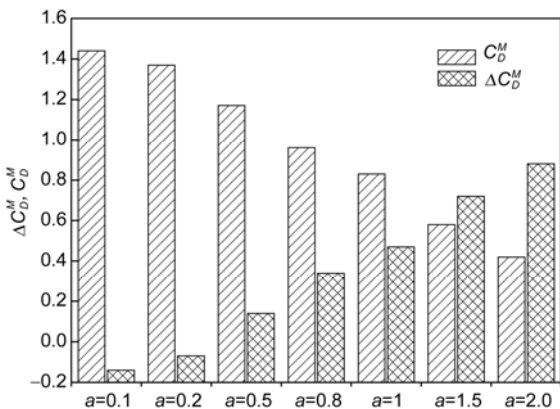

Figure 15 Comparison of electric power consumption (*Pe*) and net drag savings (ΔC_D^M).

saving ΔC_D^M to the electric power expenditure *Pe* and the efficiency of the input power in drag reduction could be observed. Therefore, considering the energy cost, an optimum point of $\alpha=0.5$ could be found where we obtain the maximum drag reduction for per Watt of *Pe*. Moreover, it is

Figure 14 Variations of mean drag coefficient and net drag savings.

Figure 16 Proportion of ΔC_D^M to *Pe* at different rotating rates.

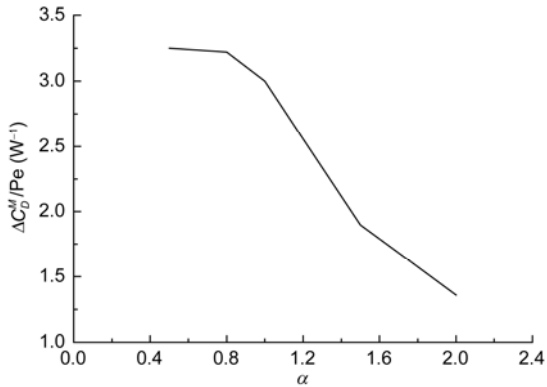necessary to consider the whole efficiency of the control method by heat transfer analysis in the following section.

3.6 Heat transfer results

It is presented in this section the heat transfer results of the main cylinder with control for different rotation rates of α at *Re*=200 and *Pr*=7.02.

Firstly, the accuracies of the present heat transfer model and methods are validated. A number of observers have measured the mean heat transfer coefficient for flow over a single cylinder. A correlation for a cylinder at uniform temperature (*Ts*) in cross-flow applied to liquids and gases has been proposed by Zukauskas [34] as follows:

$$Nu_{\mathrm{avg}} = \frac{h_{\mathrm{avg}} D}{\lambda} = C\left(\frac{U_\infty D}{\nu}\right)^m Pr^n \left(\frac{Pr}{Pr_s}\right)^{0.25}. \qquad (8)$$

In the present study, *C*=0.51, *m*=0.5, and *n*=0.37.

In addition, the local Nusselt number and average Nusselt number are defined as follows:

$$Nu_{\mathrm{loc}} = \frac{h_x D}{\lambda}, \quad Nu_{\mathrm{avg}} = \int Nu_x \mathrm{d}x. \qquad (9)$$

The predicted average Nusselt number of the present computational model is compared with that gained by eq. (8). The deviation of Nu_{avg} is 4.88%, indicating that the model and numerical methods applied are reliable and capable of modeling the heat transfer procedure.

Figure 17 presents the comparison of the average Nusselt number and local Nusselt number on the main cylinder for different rotation rates. For counter-current rotation, the average Nusselt number increases (see Figure 17(a)). However, according to the above-mentioned results, the fluid forces on the main cylinder also increase obviously for counter-current rotation. As for the case of co-current rotation, the average Nusselt number of the main cylinder is slightly lower than that of the isolated cylinder when the rotation rate is relatively small, i.e. α=0.5 (see Figure 17(a)). When higher rotation speeds are imposed on the control

cylinders, the average Nusselt number increases remarkably. In addition, it is worth noting that the local Nusselt number has two sharp peaks in the circumferential distribution in comparison with the single cylinder case (see Figure 17(b)). The two peaks of Nusselt number locate in the adjacent zone of the two subsidiary control cylinders (θ=±120°). The main reason is that the existence of the two small rotating cylinders enhances largely the flow instability around them, thus facilitates heat transfer. The two peaks make a paramount contribution to the augment of the average Nusselt number. It is observed in the local Nusselt number distribution that the heat transfer is slightly weakened in comparison with the single cylinder case in the front and rear zones of the cylinder. However, the local heat transfer enhancement near the two rotating cylinders far outweighs the little deterioration and can compensate for it. Therefore, the active control facilitates the total heat transfer even though the local heat exchanging process is slightly weakened. In general, for the purpose of both drag reduction and heat transfer enhancement, a co-current rotation of the subsidiary cylinders with a higher rotating speed is favorable. In the simulation, for α>0.5, the increment of the total heat transfer (average Nusselt number) for α=1.0 and 1.5 are 5.26% and 15.7%, respectively if they are compared with that single cylinder case.

Figure 18 shows the instantaneous isotherm patterns around the cylinder with and without control for different co-current rotation rates. As observed from these profiles, the isotherm patterns in the flow wake are greatly influenced by the rotation speed. As previously observed, the instability in wake region is suppressed with the increasing rotation rate.

4   Conclusions

In the present study, the unsteady laminar flow past a circular cylinder with attached control cylinders is numerical studied. Simulations are carried out at a Reynolds number of 200. The influences of different rotation directions and rates of the two rotating cylinders on fluid forces, flow field structures as well as heat transfer characteristics are comprehensively presented. On the basis of the numerical results, the following conclusions can be made.

1) The rotation direction of attached cylinders has great influence on the flow structure as well as the fluid forces of cylinder flow. The co-current rotation can help suppress vortex shedding and reduce the drag and lift forces. The vortex formation is delayed and weakened because of the momentum injection generated by the two rotating cylinders. For α=2.4, the vortex shedding is completely suppressed and the drag acting on the main cylinder is reduced by 77.63%, as compared with single cylinder, and the corresponding lift force is close to 0. Whereas for counter-stream rotation, both the lift and drag forces increase.
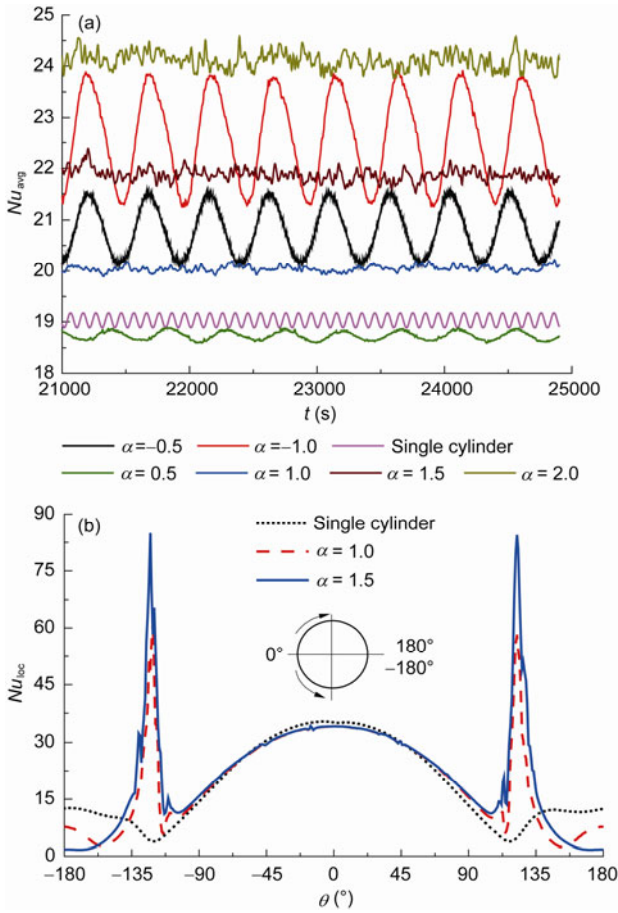
Figure 17 Comparison of Nusselt numbers on the main cylinder for different rotation rates. (a) Time histories of average Nusselt number on the main cylinder; (b) circumferential distributions of local Nusselt number.

2) The percentage of pressure component of drag force decreases gradually with the increasing co-current rotation rate $(+\alpha)$, while the percentage of friction drag increases. For counter-stream rotation $(-\alpha)$, the changing tendency of pressure and friction components is quite the contrary. The pressure differences on the main cylinder surface reduce obviously between the front and rear, and upper and lower cylinder walls, especially for a larger co-current rotation rate.

3) It is found that the total cost function has an optimum which depends on the balance between energy saved by momentum injection and energy expenditure in activating the control cylinders.

4) The average Nusselt number on the main cylinder with control increases with the rotation rate and better heat transfer performance is observed for a relatively higher rotation rate $(\alpha>0.5)$, as compared with an isolated cylinder. In addition, two peaks which locate in the adjacent zone of the two subsidiary control cylinders $(\theta=\pm120°)$ are found in the circumferential distribution of local Nusselt number, which contribute most to the increase of the average Nusselt number and compensate for the little deterioration of local Nusselt number in the front and rear zones of the main
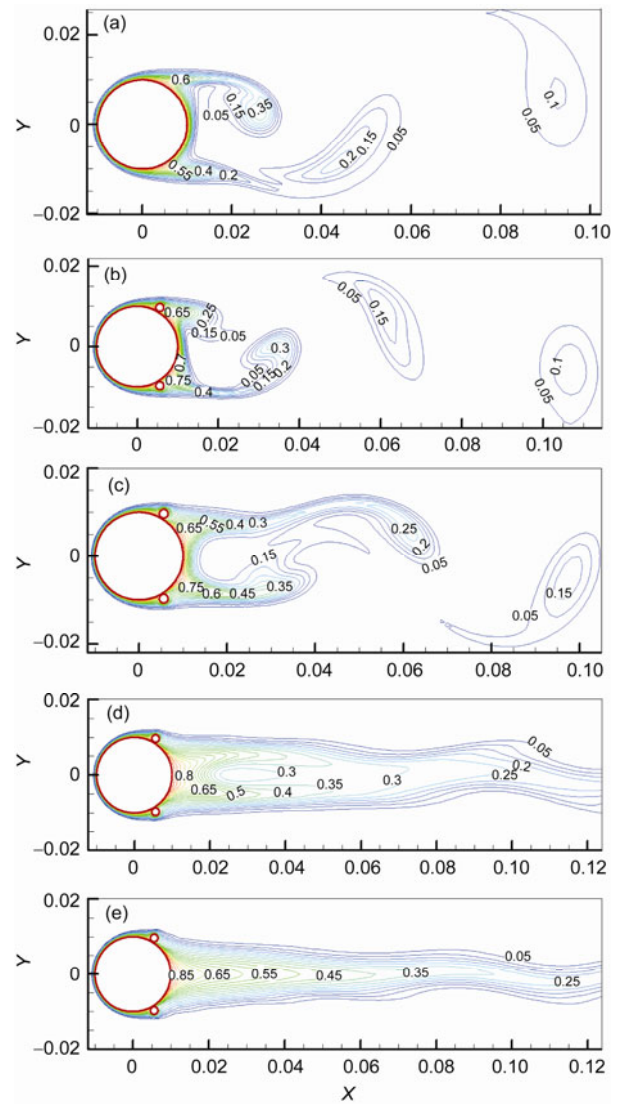
Figure 18 Isotherm profiles of cylinder with and without control for different co-current rotation rates. (a) Single cylinder; (b) $\alpha=0.5$; (c) $\alpha=1.0$; (d) $\alpha=1.5$; (e) $\alpha=2.0$.

cylinder. The main reason is that the existence of the two small rotating cylinders enhances largely the flow instability around them and thus facilitates heat transfer.

Nomenclature

a	thermal diffusion coefficient $(=\lambda/(\rho c_p))$, m^2/s;
C_D	drag coefficient, dimensionless;
C_D^M	mean value of drag coefficient, dimensionless;
C_f	friction coefficient, dimensionless;
C_L	lift coefficient, dimensionless;
C_L^A	amplitude of lift coefficient, dimensionless;
C_p	pressure coefficient, dimensionless;
c_p	specific heat capacity, J/(kg K);
D	diameter of the main circular cylinder, m;
d	diameter of the two small cylinders, m;

F_D drag force, N;

F_L lift force, N;

g gap between main cylinder and attached cylinders, m;

h distance between up (down) boundary and the cylinder center line, m;

L_1 distance between main cylinder center and inlet boundary, m;

L_2 distance between main cylinder center to outlet boundary, m;

L distance from the cylinder center, m;

Nu Nusselt number, dimensionless;

Nu_{avg} average Nusselt number, dimensionless;

Nu_{loc} local Nusselt number, dimensionless;

Pr Prandtl number, dimensionless;

p pressure, Pa;

p_{ref} reference pressure, Pa;

Pe electric power consumption, W;

Re Reynolds number ($= U_\infty D/\upsilon$), dimensionless;

T temperature, K;

t time, s;

U_∞ free-stream velocity, m/s;

u velocity component in x direction, m/s;

v velocity component in y direction, m/s;

x transverse coordinate;

y longitudinal coordinate.

Greek symbols

α rotation rate ($= \omega D / 2U_\infty$), dimensionless;

β proportional parameter, W/ (rad s^{-1})^2;

θ angle to the upstream vector direction;

$\varDelta$ increment;

ρ density, kg/m^3;

τ_w shear stress, N/m;

λ heat conductivity, W/(m K);

υ kinematic viscosity, m^2/s;

ω angular velocity, rad/s.

Self-defined symbols

$+\alpha$ co-current rotation;

$-\alpha$ counter-current rotation.

1   Park D S, Ladd D M, Hendricks E W. Feedback control of von Karman vortex shedding behind a circular cylinder at low Reynolds numbers. Phys Fluids, 1994, 6: 2390–2405

2   Gunzburger M D, Lee H C. Feedack control of vortex shedding. Trans ASME J Appl Mech, 1996, 63: 828–835

3   Fransson J H M, Konieczny P, Alfredsson P H. Flow around a porous cylinder subject to continuous suction or blowing. J Fluid Struct, 2004, 19: 1031–1048

4   Fujisawa N, Asano Y, Arakawa C, et al. Computational and experimental study on flow around a rotationally oscillating circular cylinder in a uniform flow. J Wind Eng Ind Aerody, 2005, 93: 137–153

5   Ma L Q, Feng L H. Experimental investigation on control of vortex shedding mode of a circular cylinder using synthetic jets placed at

stagnation points. Sci China Tech Sci, 2013, 56: 158–170

6   Kwon K, Choi H. Control of laminar vortex shedding behind a circular cylinder using splitter plates. Phys Fluids, 1996, 8: 479–486

7   Darekar R M, Sherwin S J. Flow past a bluff body with a wavy stagnation face. J Fluid Struct, 2001, 15: 587–596

8   Lee S J, Lee S I, Park C W. Reducing the drag on a circular cylinder by upstream installation of a small control rod. Fluid Dyn Res, 2004, 34(4): 233–250

9   Hwang J, Yang K. Drag reduction on a circular cylinder using dual detached splitter plates. J Wind Eng Ind Aerody, 2007, 95: 551–564

10 Malekzadeh S, Sohankar A. Reduction of fluid forces and heat transfer on a square cylinder in a laminar flow regime using a control plate. Int J Heat Fluid Fl, 2012, 34: 15–27

11 Williamson C H K, Roshko A. Vortex formation in the wake of an oscillating cylinder. J Fluids Struct, 1998, 2: 355–381

12 Lu X Y, Sato J. A numerical study of flow past a rotationally oscillating circular cylinder. J Fluid Struct, 1996, 10: 829–849

13 Baek S J, Sung H J. Numerical simulation of the flow behind a rotary oscillating circular cylinder. Phys Fluids, 1998, 10: 869–876

14 Cheng M, Chew Y T, Luo S C. Numerical investigation of a rotationally oscillating cylinder in mean flow. J Fluid Struct, 2001, 15: 981–1007

15 Srinivas K, Fujisawa N. Effect of rotational oscillation upon fluid forces about a circular cylinder. J Wind Eng Ind Aerody, 2003, 91: 637–652

16 Modi V J. Moving surface boundary-layer control: A review. J Fluid Struct, 1997, 11: 627–663

17 Mokhtarian F, Modi V J. Fluid dynamics of airfoils with moving surface boundary-layer control. J Aircr, 1988, 25: 163–169

18 Ott E, Grebogi C, Yorke J A. Controlling chaos. Phys Rev Lett, 1990, 64(11): 1196–1199

19 Wei G W. Synchronization of single-side locally averaged adaptive coupling and its application to shock capturing. Phys Rev Lett, 2001, 86(16): 3542–3545

20 Tang G, Guan S, Hu G. Controlling flow turbulence with moving controllers. Eur Phys J B, 2005, 48: 259–264

21 Tang G, Hu G. Controlling flow turbulence using local pinning feedback. Chin Phys Lett, 2006, 23(6): 1523–1526

22 Muddada S, Patnaik B S V. An active flow control strategy for the suppression of vortex structures behind a circular cylinder. Eur J Mech B-Fluid, 2010, 29: 93–104

23 Strykowski P J, Sreenivasan K R. On the formation and suppression of vortex shedding at low Reynolds numbers. J Fluid Mech, 1990, 218: 71–107

24 Lienhard J. Synopsis of lift, drag and vortex frequency data for rigid circular cylinder. Washington State University, College of Engineering, Research Division Bulletin 300, 1966

25 Kang S, Choi H, Lee S. Laminar flow past a rotating circular cylinder. Phys Fluids, 1999, 11: 3312–3321

26 Stojkovic D, Breuer M, Durst F. Effect of high rotation rates on the laminar flow around a circular cylinder. Phys Fluids, 2002, 14(9): 3160–3178

27 Gim O S, Kim S H, Lee G W. Flow control behind a circular cylinder by control rods in uniform stream. Oc Engrg, 2011, 38(17-18): 2171–2184

28 Karabelas S J. Large eddy simulation of high-Reynolds past a rotating cylinder. Int J Heat Fluid Fl, 2010, 31: 518–527

29 Price S J, Sumner D, Smith J G, et al. Flow visualization around a circular cylinder near to a plane wall. J Fluid Struct, 2002, 16(2): 175–191

30 Fluent 6.3 User's Guide. Fluent Inc., 2006

31 Homescu C, Navon I M, Li Z. Suppression of vortex shedding for flow around a circular cylinder using optimal control. Int J Numer Meth Fluid, 2002, 38: 43–69

32 Beaudoin J F, Cadot O, Aider J L, et al. Bluff body drag reduction by extremum-seeking control. J Fluids Struct, 2006, 22: 973–978

33 Beaudoin J F, Cadot O, Aider J L, et al. Drag reduction of a bluff body using adaptive control methods. Phys Fluids, 2006, 18 (8): 085107

34 Zukauskas A A. Heat transfer from tubes in cross flow. Adv Heat Trans, 1972, 8: 93–106